


Article

Prediction of Contact Angle for Oriented Hydrophobic Surface and Experimental Verification by Micro-Milling

Yiwen Zhu ^{1,2,†}, Wei Xu ^{1,2,†}, Ziyang Cao ^{1,2,*} , Wenlu Meng ^{1,2}, Jiawei Ni ^{1,2}, Jie Pan ^{1,2} and Dong Wei ^{1,2}

¹ College of Mechanical Engineering, Suzhou University of Science and Technology, Suzhou 215009, China; 15358446337@163.com (Y.Z.); 15505223772@163.com (W.X.); mengwlyyds@163.com (W.M.); nijoy96@163.com (J.N.); p13685298420j@163.com (J.P.); 13921922404@163.com (D.W.)

² Suzhou Key Laboratory of Precision and Efficient Machining Technology, Suzhou 215009, China

* Correspondence: dukeczy@nuaa.edu.cn; Tel.: +86-0512-6832-1707

† These authors contributed equally to this work.

Abstract: The rectangular microgroove surfaces have obvious anisotropy, which can control the movement of water droplets in parallel and vertical directions. Based on such a property, anisotropic functional surfaces are expected to have potential applications in the fields of droplet-oriented delivery and microfluidics. Micro-milling can accurately adjust the dimension of microstructures, which is convenient to explore the optimal micro-structural parameters. In this study, the non-composite and composite state prediction models of contact angle on the oriented hydrophobic surface were established based on minimum Gibbs free energy, and the effect of micro-structural dimension parameters on contact angle was investigated. Then, the rectangular microgroove structure on 316 L stainless steel was prepared using micro-milling. The composite state prediction model of contact angle was found to be more consistent with the actual situation, and reducing the width of the convex platform was beneficial to increasing the contact angle. In particular, the contact angle in the parallel direction reached 146.5° when the width of the convex platform was 60 μm, and the accuracy of the prediction model was 98.4%. The proposed prediction models of contact angle provide a theoretical basis for designing and preparing oriented hydrophobic surfaces.

Keywords: oriented hydrophobicity; contact angle; rectangular microgroove structure; Gibbs free energy; micro-milling



Citation: Zhu, Y.; Xu, W.; Cao, Z.; Meng, W.; Ni, J.; Pan, J.; Wei, D. Prediction of Contact Angle for Oriented Hydrophobic Surface and Experimental Verification by Micro-Milling. *Coatings* **2023**, *13*, 1305. <https://doi.org/10.3390/coatings13081305>

Academic Editor: Carlo Antonini

Received: 14 June 2023

Revised: 8 July 2023

Accepted: 17 July 2023

Published: 25 July 2023



Copyright: © 2023 by the authors. Licensee MDPI, Basel, Switzerland. This article is an open access article distributed under the terms and conditions of the Creative Commons Attribution (CC BY) license (<https://creativecommons.org/licenses/by/4.0/>).

1. Introduction

For billions of years, organisms have evolved various microstructures on the surface of their bodies to adapt to the living environment and shown unique liquid-repellent behaviors. A typical phenomenon is the “Lotus Leaf Effect” [1]. Barthlott and Neinhuis [2] first observed the presence of micron-sized mastoid structures on the lotus leaf’s surface, revealing the relationship between microstructure and hydrophobicity. In recent years, microtopologies such as square [3], cylinder [4], and inverted trapezoid [5] have been proposed to imitate lotus leaves, but these microstructures can only shape isotropic hydrophobic surfaces. Unlike lotus leaves, the microstructures on the rice leaf surface have directional hydrophobicity. The grooved microstructure on the rice leaf’s surface does not allow water droplets to fall from the side of the leaves, and water droplets can only be discharged longitudinally to the roots to provide the water needed for growth [6]. Inspired by this, a functional surface that limits water flow in a specific direction can be designed and will play an important role in cardiovascular stents [7], fluid drag reduction [8,9], droplet-oriented delivery [10], microfluidic devices [11], etc.

It is noteworthy that vascular stent materials are used to treat cardiovascular diseases caused by thrombosis in the medical field. However, most of the vascular stent materials themselves do not have anti-blood adhesion properties and easily interact with the components in the blood, resulting in the formation of secondary thrombosis. Studies have

proven that hydrophobic surfaces could reduce the adhesion of microimplants to bacteria and blood, thereby reducing the risk of vascular restenosis [12]. Therefore, improving the oriented hydrophobicity of microimplants in the direction of blood flow is very important for its clinical application.

Some geometric microstructures have been proven to form oriented hydrophobic surfaces. Zhou et al. [13] devised the periodic asymmetric multi-directional stairway (AMDS) pattern on the sample surfaces with the same riser height (RH) and unique unequal tread depth (TD) in four directions and superimposed the laser-induced nano-structures on the surface of the AMDS. They found that the water droplets in the four regions of the surface slid in turn when they reached their respective critical angles with the increase in the inclination angle, thus realizing the anisotropic sliding of water droplets in different directions. Lian et al. [14] established a three-level microstructure with sub-millimeter-micron-nanometer characteristics on the surface of aluminum alloy by imitating rice leaves and found that micron and nano-structures were the root causes of superhydrophobicity while a sub-millimeter groove array structure caused water droplets to exhibit anisotropic wettability in parallel and vertical directions. Fang et al. [15] constructed periodic microgrooves based on polydimethylsiloxane to achieve bidirectional wettability of the surface. Xu et al. [16] reported a three-scale structure built on Ti-6Al-4V with sub-millimeter grooves, micro-pits, and nano-grid features and found that the groove features played an important role in oriented hydrophobicity. Long et al. [17] designed a groove-like microstructure based on a copper surface and studied the effect of surface morphology on the wetting state and directional sliding of water droplets. Zhu et al. [18] prepared the ordered binary microgroove structures on silicon wafers and found that the surface had good anisotropy to water droplets. Although the abovementioned studies have constructed directional microstructures, the corresponding prediction models of contact angle have not been established and the most reasonable dimension parameters have not been clearly given. In particular, because the rectangular microgroove structure can locally control the directional hydrophobicity of the surface, it has great potential in basic research and application [19]. Therefore, it is necessary to establish prediction models of contact angle for this microstructure. However, the acquisition of this microstructure faces some challenges, such as the difficulty of accurate preparation in large periods and large depths.

Some strategies for preparing hydrophobic surfaces have been proposed, including chemical methods [20–22] and micromachining methods [23–25]. Chemically, Wei et al. [26] combined hydrochloric acid etching with stearic acid modification to shape dense hydrophobic microstructures on the surface of a magnesium alloy. Wang et al. [27] constructed water-repellent composite coatings on a variety of substrates, which was attributed to the electrodeposition-polymer composite technology they developed. Mokhtari et al. [28] reported a new method combining anodic oxidation and stearic acid modification to construct microstructures on aluminum alloys and obtained hydrophobic surfaces at the cathode. However, the shape and geometry of the microstructures generated by chemical methods were random, and the wettability of the surface could not be accurately regulated. In addition, these processes usually involve complex cleaning and coating steps, as well as the use of dangerous chemical reagents and gas masks [20,27].

For micromachining methods, Volpe et al. [29] mapped square, circular, and triangular groove lattice microstructures based on a femtosecond laser. Chen et al. [30] constructed semicircular groove microstructures on the surface of SiCp/Al using WEDM and obtained controllable wear-resistant hydrophobic surfaces. Although both methods can generate some regular micro-features, the chemical composition and properties of the surface are easily changed due to the ablation of the substrate [23]. In addition, nanosecond laser will produce a high heat effect due to the low processing throughput, and WEDM is prone to generating irregular recast melting layers [30], which results in the formation of multimodal rough structures [31]. It is worth noting that with the decrease in machine tool runout and milling cutter diameter, it has become a reality to construct surface microstructures using micro-milling technology [32]. It is easier for micro-milling to achieve high-precision

automatic control and obtain repetitive micro-features with large periods and depths, which provides favorable technical support for exploring the relationship between contact angle and micro-structural dimension.

In this work, the prediction models of contact angle were established by combining Gibbs free energy and a rectangular microgroove structure, and the variation of contact angle with micro-structural dimension parameters was discussed. Furthermore, the precise preparation of a rectangular microgroove structure on 316L stainless steel was achieved using micro-milling technology. The reliability of the prediction models was verified by characterizing the contact angles of the micro-structural surfaces. In addition, the experimental results showed that reducing the width of the convex platform contributes to increasing the contact angle.

2. Establishment of Contact Angle Prediction Model

2.1. Theoretical Basis of Hydrophobicity

Wettability is a property of the material surface characterized by water contact angle (WCA) [33]. The hydrophobic surface repels water droplets, resulting in a corresponding WCA higher than 90° [34,35]. In 1805, Thomas Young [36] proposed the contact angle model for smooth surfaces in terms of thermodynamic equilibrium:

$$\cos\theta_Y = \frac{\sigma_{SV} - \sigma_{SL}}{\sigma_{LV}} \quad (1)$$

where θ_Y is the contact angle, and σ_{SV} , σ_{SL} and σ_{LV} are the interfacial tensions of the solid–gas phase, solid–liquid phase, and liquid–gas phase, respectively, as shown in Figure 1.

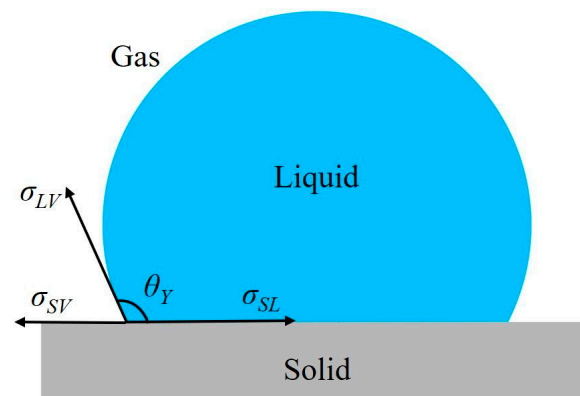


Figure 1. Schematic diagram of droplet contact angle on the smooth surface.

The material surface usually has a certain roughness. Therefore, Wenzel [37] and Cassie [38] proposed another model of contact angle considering roughness. Wenzel droplets infiltrated the microgroove, and there was no liquid–gas contact at the bottom of the droplets; hence this model is also called the non-composite state model. However, the Cassie droplets did not infiltrate the microgroove, and the bottoms of the droplets were in contact with both the convex platform and the air; hence this model is also called the composite state model.

Water droplets placed on the solid surface are subject to the balance of surface tension and gravity, which is negligible if the gravity is very small relative to the surface tension. The action of the surface tension causes the water droplets to be fixed on the solid surface. The water droplets are in the most stable state when the Gibbs free energy of the entire wetting system is the smallest and the contact angle is the apparent contact angle of the water droplets. Studies have shown that surface free energy refers to the partial derivative of Gibbs free energy to the area at constant temperature and pressure [39], which is numerically equal to surface tension. If the dimension of the water droplet is small, the water droplet will be in a spherical state under the action of surface tension. It is assumed

that the cross-section area of the water droplets is constant. Therefore, the Gibbs free energy of water droplets in the two-dimensional cross-section is expressed as the contact force, as shown in Equation (2):

$$F = \gamma_{SL}L_{SL} + \gamma_{SV}L_{SV} + \gamma_{LV}L_{LV} \tag{2}$$

where F is the contact force; γ_{SL} , γ_{SV} and γ_{LV} are the interfacial free energy of the solid–liquid, solid–gas, and liquid–gas interfaces, respectively; and L_{SL} , L_{SV} , and L_{LV} are the length of the solid–liquid, solid–gas, and liquid–gas contact lines, respectively.

2.2. Establishment of the Non-Composite State Model

The non-composite state model makes the hydrophilic surface more hydrophilic and the hydrophobic surface more hydrophobic [37]. Therefore, the hydrophilic surface and the hydrophobic surface will present the two cases shown in Figure 2.

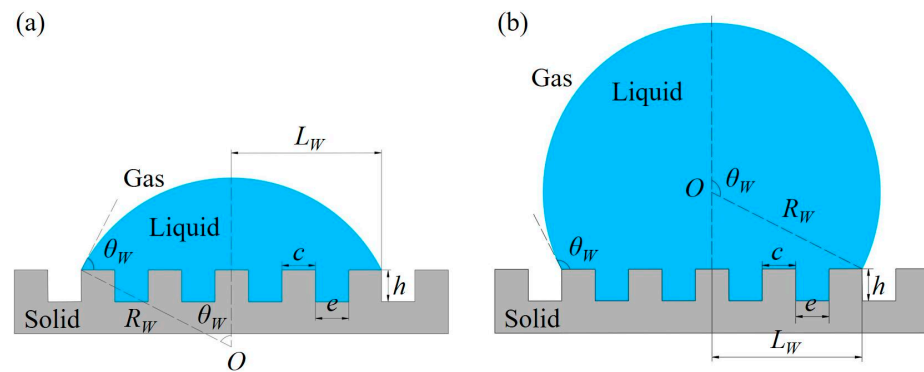


Figure 2. Droplet diagram of the non-composite state model: (a) hydrophilic surface; (b) hydrophobic surface.

According to Figure 2, c represents the convex platform width of the rectangular microgroove structure, e represents the spacing width of the rectangular microgroove structure, and h represents the height of the convex. L_W is the distance from the edge of the three-phase contact line to the center of the contact line, θ_W is the non-composite state contact angle, and R_W represents the radius of the water droplet. Therefore, the number of convex platforms can be expressed as Equation (3):

$$m = \frac{2L_W - c}{c + e} \tag{3}$$

L_{SL} , L_{LV} , and L_{SV} can be expressed as Equations (4)–(6), respectively:

$$L_{SL} = (m + 1)c + m(2h + e) = \frac{2L_W + e}{c + e}c + \frac{2L_W - c}{c + e}(2h + e) \tag{4}$$

$$L_{LV} = 2\theta_W \frac{L_W}{\sin \theta_W} \tag{5}$$

$$L_{SV} = L_{total} - L_{SL} \tag{6}$$

where L_{total} is the total contact line length of water droplets on the solid surface, with a constant value.

Putting Equation (6) into Equation (2), the contact force can be expressed as Equation (7):

$$F = \gamma_{SL}L_{SL} + \gamma_{LV}L_{LV} + \gamma_{SV}(L_{total} - L_{SL}) \tag{7}$$

The area constraint of the wetting system is:

$$S = \theta_W \frac{L_W^2}{\sin^2 \theta_W} - \frac{L_W^2}{\tan \theta_W} + \frac{2L_W - c}{c + e}eh \tag{8}$$

Since only the length of the contact line between the water droplet and the microgroove changes and the area of the cross-section is constant, there is:

$$dS = 0 \tag{9}$$

Putting Equation (8) into Equation (9) gives:

$$\frac{d\theta_W}{dL_W} = \frac{2eh \sin^2_{\theta_W} + (c + e)L_W(2\theta_W - \sin 2\theta_W)}{2(c + e)L_W^2(\theta_W \cot \theta_W - 1)} \tag{10}$$

The Gibbs free energy is the smallest when the wetting system is most stable and the contact force is minimum, so there is:

$$dF = 0 \tag{11}$$

Putting Equation (7) into Equation (11) gives:

$$\gamma_{SL}dL_{SL} + \gamma_{LV}dL_{LV} - \gamma_{SV}dL_{SL} = 0 \tag{12}$$

Combining Equations (1), (4), (5), (10), and (12), there is:

$$\cos \theta_Y = \frac{\gamma_{SV} - \gamma_{SL}}{\gamma_{LV}} = \frac{dL_{LV}}{dL_{SL}} = \frac{(c + e)\cos \theta_W}{c + e + 2h} \tag{13}$$

In the parallel observation direction, the relationship between the non-composite state contact angle and the micro-structural dimension parameters can be expressed as Equation (14):

$$\theta_{WP} = \arccos \left[\left(1 + \frac{2h}{c + e} \right) \cos \theta_Y \right] \tag{14}$$

In the vertical observation direction, the non-composite state contact angle can be expressed as Equation (15):

$$\theta_{WV} = \arccos \left[\left(1 + \frac{2h}{c} \right) \cos \theta_Y \right] \tag{15}$$

2.3. Establishment of the Composite State Model

Water droplets in contact with solids are subjected to additional pressures caused by downward hydrostatic pressure and additional pressure caused by contact line tension [40]. According to the phenomenon of capillary action, the actual liquid–gas contact line between the water droplet and the microstructure is not straight. There is a certain angle at the contact position, which is equal to the intrinsic contact angle of the solid, as shown in Figure 3.

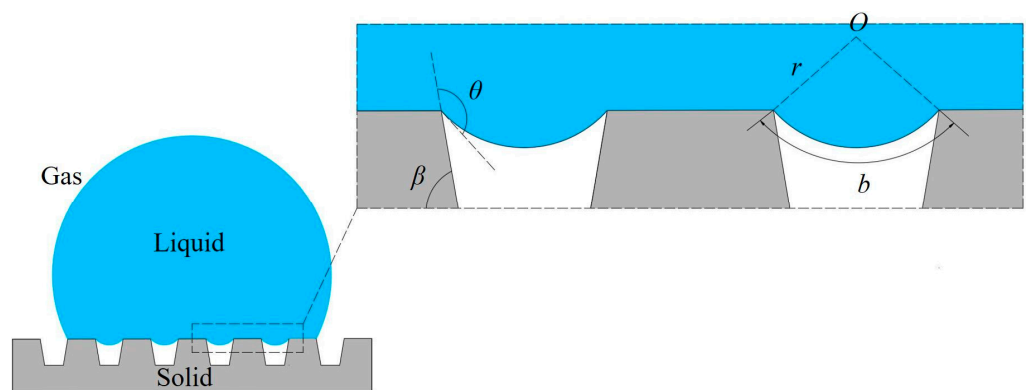


Figure 3. Schematic diagram of liquid–gas contact line at microstructure.

From Figure 3, r is the radius of curvature, θ is the intrinsic contact angle, β is the inclined wall angle of the microgroove, and b is the length of the actual liquid–gas contact line. According to the geometric relationship, there are:

$$r = \frac{e}{2\sin(\theta + \beta)} \tag{16}$$

$$b = (\pi - \theta - \beta) \frac{e}{\sin(\theta + \beta)} \tag{17}$$

In this work, $\beta = 90^\circ$, so there is:

$$b = \frac{\pi - 2\theta}{2 \cos \theta} e \approx e \tag{18}$$

Therefore, the actual liquid–gas contact line can be regarded as approximately a straight line, as shown in Figure 4.

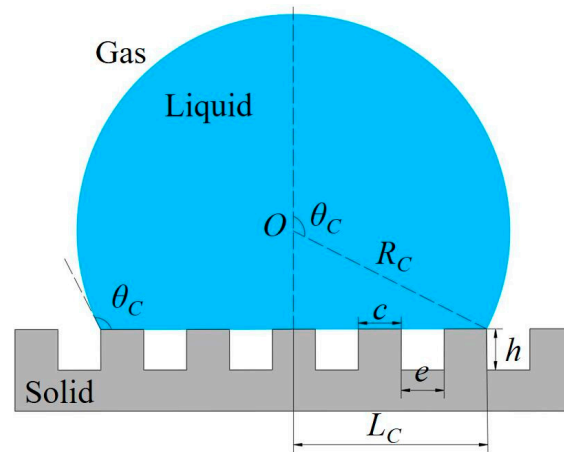


Figure 4. Droplet diagram of the composite state model.

According to Figure 4, L_C is the distance from the edge of the three-phase contact line to the middle of the contact line and θ_C is the composite state contact angle. Therefore, the number of convex platforms can be expressed as Equation (19):

$$m = \frac{2L_C - c}{c + e} \tag{19}$$

L_{SL} and L_{LV} can be expressed as Equations (20) and (21), respectively:

$$L_{SL} = \frac{2L_C + e}{c + e} c \tag{20}$$

$$L_{LV} = 2\theta_C \frac{L_C}{\sin \theta_C} + \frac{2L_C - c}{c + e} e \tag{21}$$

The area constraint of the wetting system is:

$$S = \theta_C \frac{L_C^2}{\sin^2 \theta_C} - \frac{L_C^2}{\tan \theta_C} \tag{22}$$

Putting Equation (22) into Equation (9), there is:

$$\frac{d\theta_C}{dL_C} = \frac{2\theta_C - \sin 2\theta_C}{2L_C(\theta_C \cot \theta_C - 1)} \tag{23}$$

Combining Equations (1), (12), (20), (21) and (23), there is:

$$\cos \theta_Y = \frac{dL_{LV}}{dL_{SL}} = \frac{(c + e)\cos \theta_C + e}{c} \quad (24)$$

In the parallel observation direction, the relationship between the composite state contact angle and the micro-structural dimension parameters can be expressed as Equation (25):

$$\theta_{CP} = \arccos\left(\frac{c \cos \theta_Y - e}{c + e}\right) \quad (25)$$

In the vertical observation direction, the composite state contact angle can be expressed as Equation (26):

$$\theta_{CV} = \theta_Y \quad (26)$$

The model established by Equations (14) and (25) was numerically simulated with MATLAB (Matlab R2016b, 2016, MathWorks, Natick, MA, USA) and the three-dimensional surface diagram of the relationship between contact angle and micro-structural dimension parameters was obtained, as shown in Figure 5. It can be seen that the contact angles of the non-composite state and the composite state are increasing functions of the eigenvalue e , but the non-composite state contact angle increases and the composite contact angle state decreases when the eigenvalue c increases. In particular, the composite state contact angle increases relatively greatly when the eigenvalue c decreases.

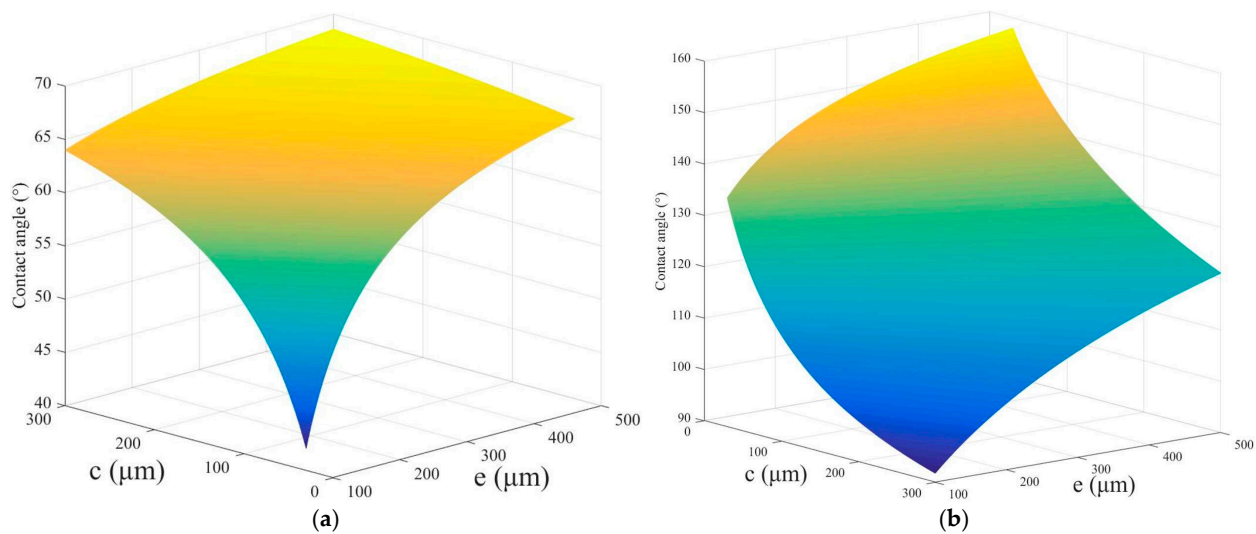


Figure 5. Correlation between contact angle and structural parameters: (a) non-composite state model; (b) composite state model.

3. Experimental Verification

3.1. Experimental Conditions and Methods

316 L stainless steel sheets (Shanghai Luhao Metal Group, Shanghai, China) with a dimension of 16 mm × 5 mm × 1 mm were selected for experimental validation of the prediction models. 316 L stainless steel is widely used in the biomedical field due to its excellent corrosion resistance and biocompatibility. Before machining, the surface of the material was polished to ensure machining accuracy. It is worth mentioning that due to the small thickness of the sample, it cannot be directly clamped onto the micro-milling machine. Therefore, we proposed to use brass with the dimension of 40 mm × 16 mm × 16 mm as the substrate. Firstly, the face milling cutter with a diameter of 4 mm was used to roughen its surface to form a positioning datum. Then, the 316L stainless steel polished sheets were ultrasonically cleaned with absolute alcohol and deionized water for 5 min to remove impurities and oil stains on the surface, and the cleaned samples were bonded to the positioning datum with 502 glue. After completing the

abovementioned preparation work, a micro milling cutter was used to process the microstructure on the surface of the samples. The preparation process of the microstructure is shown in Figure 6.

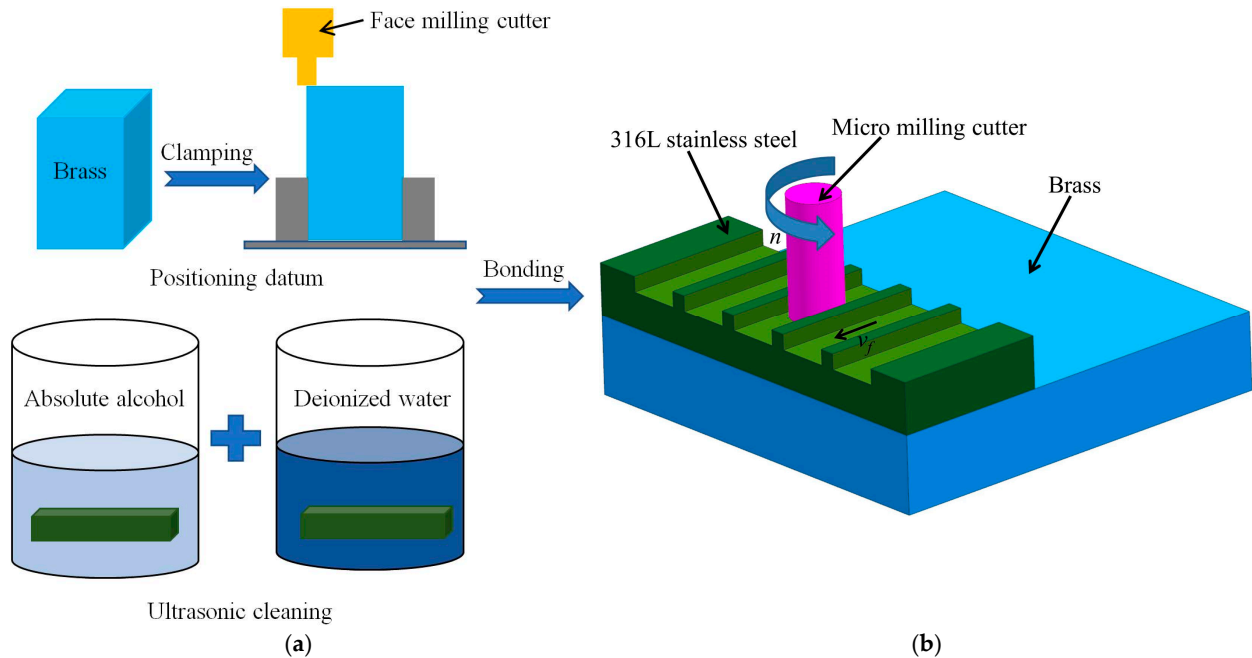


Figure 6. The preparation flow chart of microstructure on 316 L stainless steel: (a) fixation of 316 L stainless steel; (b) preparation of microgroove structure.

The cutting system used in this work was a vertical boring-milling machining center. The NACO-ALTISIN (Shanghai, China) coated micro milling cutter with a tool diameter of 0.3 mm was selected. Figure 7 is the schematic diagram of the micro-milling system. The spacing width e and the convex height h were fixed to 350 μm and 100 μm , respectively. The wettability of the stainless steel surface was verified by changing the convex platform width c , and its values were 60 μm , 80 μm , 100 μm , 130 μm , 160 μm , and 200 μm , respectively. The cutting parameters of the microstructure are listed in Table 1. It is worth noting that this is the final result of a large number of parameter optimization experiments. After cutting, the samples were ultrasonically cleaned with absolute alcohol and deionized water for 5 min again. Finally, all samples were dried and sealed with metallographic tape to wait for the next measurement.

3.2. Characterization and Measurement

The apparent morphology of samples was characterized using the ultra-depth 3D microscope (VHX-5000, Keyence, Osaka, Japan) and the scanning electron microscope (EM-30AX+, Coxem, Daejeon, Korea). The contact angles of these samples were measured using an optical contact angle measuring instrument (JC2000D1, Powereach, Shanghai, China). The test liquid was deionized water with a volume of 4 μL . In addition, no fewer than six measurements were conducted for every sample to ensure the accuracy of the measured data.

3.3. Results and Analysis

3.3.1. Surface Morphology and Geometry Dimension

Surface morphology and geometry dimension have a great influence on wettability. Figure 8a shows the macroscopic surface topography of sample 4. It was observed that some regular periodic rectangular microgroove features were created on the 316 L stainless steel by micro-milling, and these microstructures were arranged in orderly and uniform

dimensions. Figure 8b is the microscopic surface topography of sample 4 under the ultra-depth 3D microscope. It can be seen that the bottom of the rectangular microgroove is composed of many arc-shaped stripes in the same direction. This is because the micro milling cutter generated a circular arc after each feeding. The circular arc is also called a sub-cycloid, which reflects the change of tool path [41].

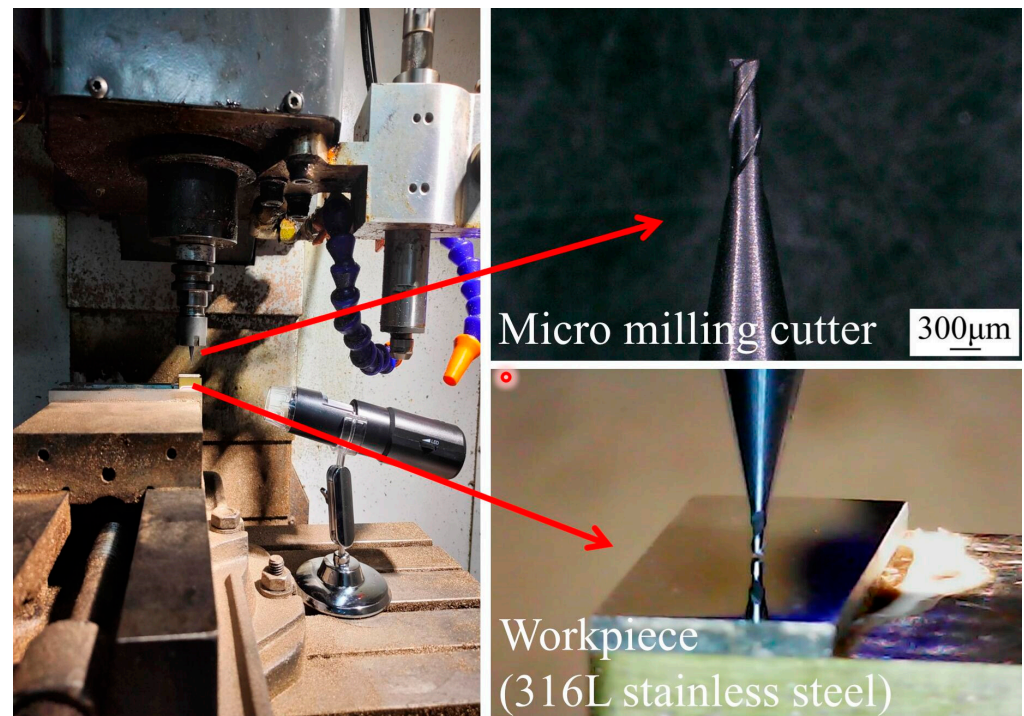


Figure 7. Schematic diagram of the micro-milling system.

Table 1. Cutting parameters in the micro-milling process.

Spindle Speed (r/min)	Feed Speed (mm/min)	Depth of Cut (μm)
17,000	25	10

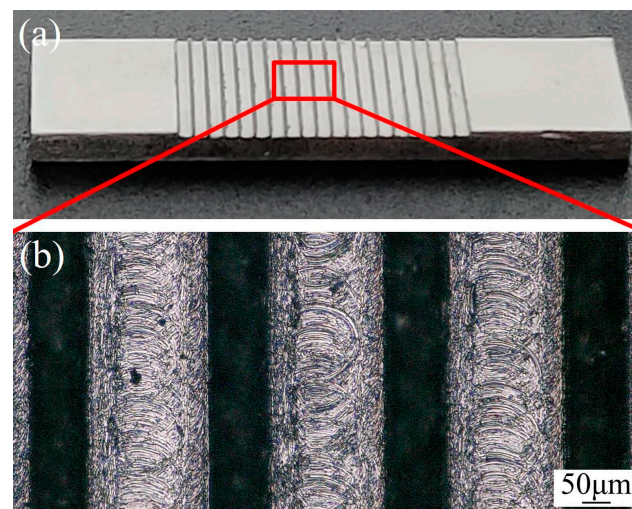


Figure 8. Surface topography of sample 4: (a) macroscopic surface; (b) microscopic surface.

Figure 9 is the outline dimension of rectangular microgrooves on the surface of sample 4 measured by the ultra-depth 3D microscope. It can be seen that the height of the convex is about 100~110 μm . This is because the tool fed downward while rotating with the spindle in the process of tool setting. Then, the tool setting process ended when the chip appeared on the surface of the sample for the first time. Note that the surface of the sample generated a certain depth when the chip was formed so the height of convex after processing was bound to be greater than the preset value. In addition, three positions of the same convex platform were measured from bottom to top, and the values were 149.52 μm , 142.56 μm , and 131.5 μm , respectively. Thus, the width of the convex platform decreased from bottom to top, which also led to increases in the corresponding spacing width. This is mainly due to the small diameter of the cutter, the large overhang of the cutter, and the chatter of the machine tool that caused the micro milling cutter to shake, and the upper part of the convex had a slight bending to both sides, leading to little stiffness [42]. It was calculated that the influence of the slight bending of the convex platform on the contact angle was only within 2° , which is almost negligible.

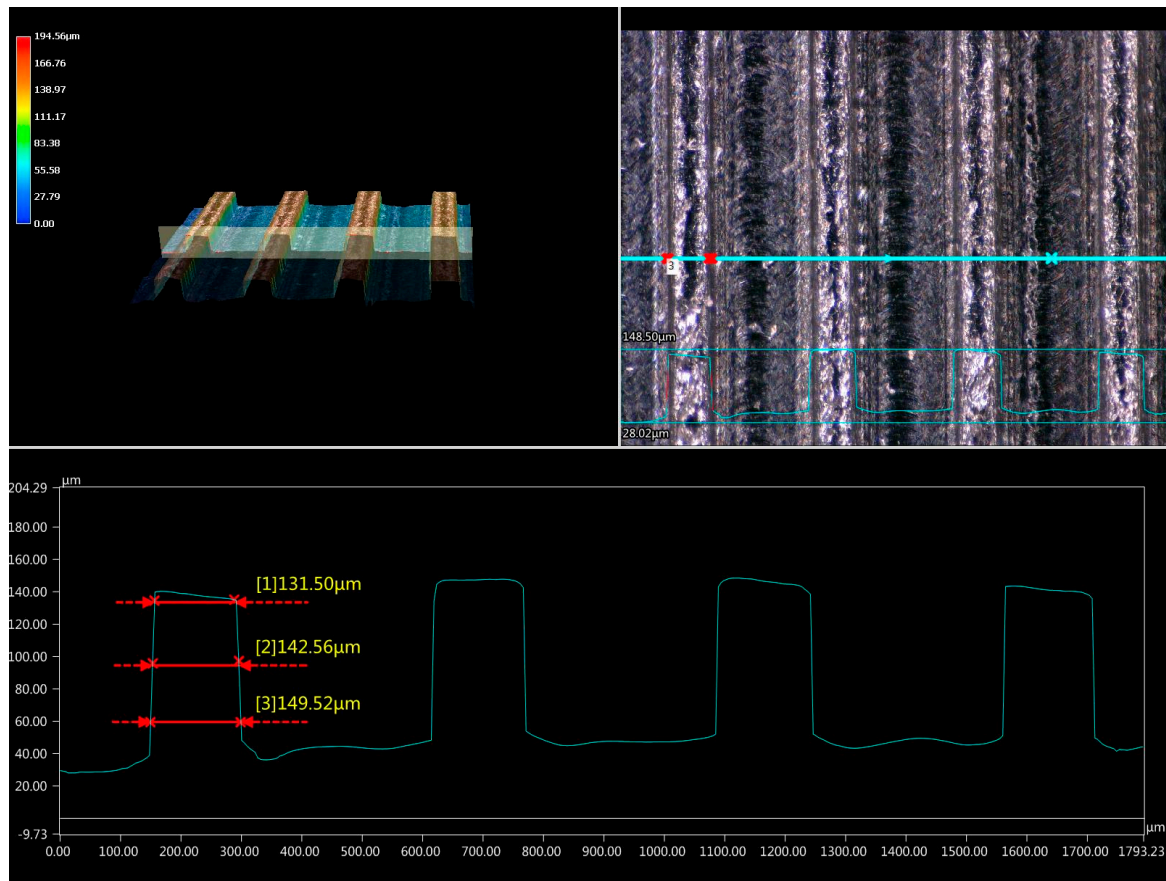


Figure 9. The outline dimension measurement diagram of rectangular microgroove of sample 4.

3.3.2. Surface Wettability

Figure 10 shows the wettability comparison of the surface before and after micro-milling. It can be seen that the surface tension of water droplets on the smooth surface is small, so it spread around. However, the surface tension of water droplets on the micro-structural surface is large, so it was supported. Figure 11 shows the contact angle of the 316 L stainless steel smooth surface, which was measured to be 72.5° .

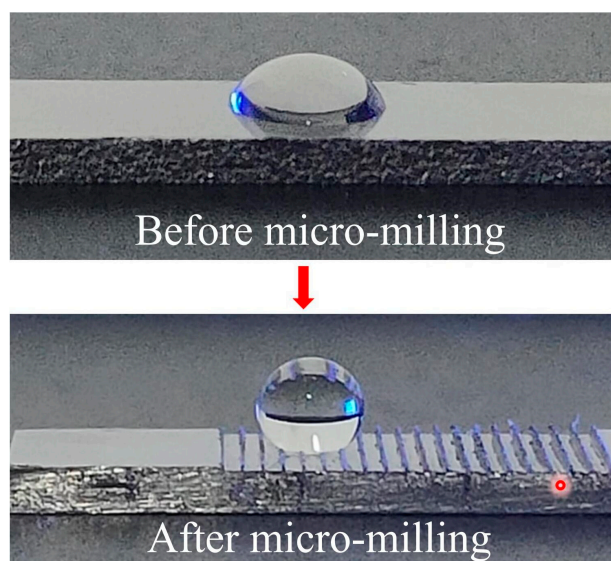


Figure 10. Variation of wettability before and after micro-milling.

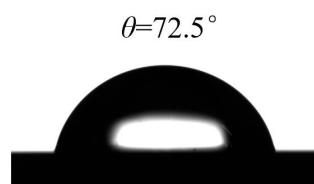


Figure 11. Contact angle of 316L stainless steel smooth surface.

Figure 12 shows the measurements of contact angles on microstructural surfaces. It can be observed that the hydrophobicity of the six samples was greatly improved compared to the smooth surface. Figure 12a shows that the contact angles in the parallel observation direction reached more than 120° and the wettability of the surfaces was changed from hydrophilic to hydrophobic. The measured contact angle in the parallel observation direction was as high as 146.5° when the width of the convex platform was 60 μm, and the accuracy of the prediction model is 98.4%. Furthermore, with the continuous increase in convex platform width, the measured contact angles in this direction showed a downward trend. The parallel contact angle decreased from 146.5° to 126.2°, with a decrease of 20.3°. In addition, it can be found from Figure 12b that although the contact angles in the vertical observation direction increased, some surfaces were still hydrophilic. This indicates that the wettability difference between the parallel and vertical observation directions is significant. The vertical contact angle decreased from 92.4° to 82.8°, with a decrease of 9.6°. Thus, the parallel contact angle changed more obviously than the vertical contact angle when the width of the convex platform changed.

To verify the reliability of the prediction models, the theoretical contact angle values under different convex platform widths are listed in Table 2 together with the experimental measurement values. Figure 13 shows the curve drawn based on the data in Table 2.

Table 2. The theoretical and experimental values of contact angle.

Sample Number	Convex Platform Width <i>c</i> (μm)	Theoretical Value of Non-Composite State θ_{WP} (Parallel)	Theoretical Value of Composite State θ_{CP} (Parallel)	Theoretical Value of Composite State θ_{CV} (Vertical)	Measured Value θ_P (Parallel)	Measured Value θ_V (Vertical)
1	60	64.2°	144.2°	72.5°	146.5°	92.4°
2	80	64.6°	139.4°	72.5°	141.1°	90.3°
3	100	65.0°	135.5°	72.5°	137.3°	87.9°
4	130	65.5°	130.5°	72.5°	134.7°	86.7°
5	160	66.0°	126.5°	72.5°	127.2°	85.3°
6	200	66.5°	122.1°	72.5°	126.2°	82.8°

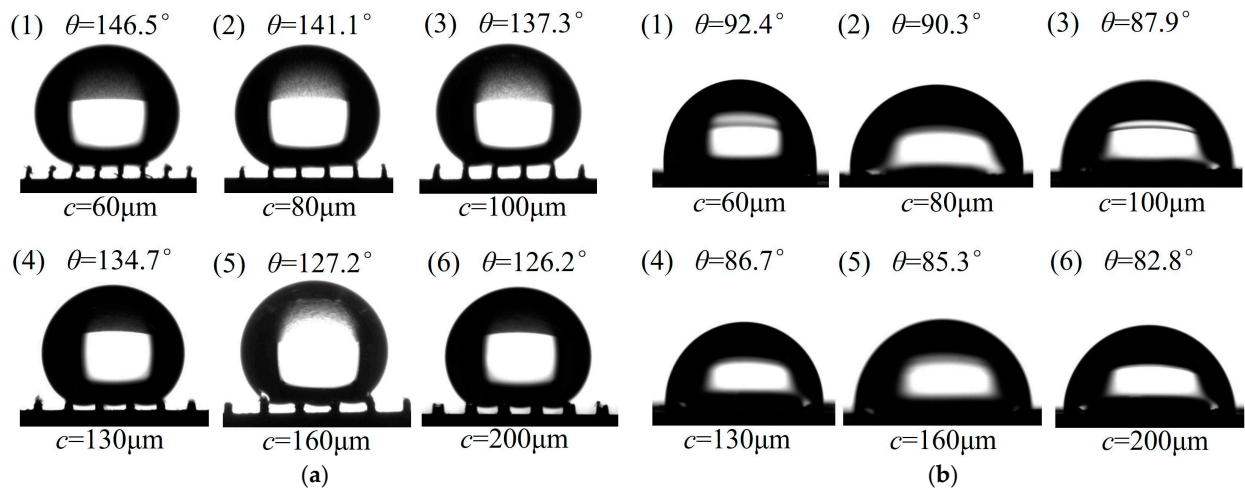


Figure 12. Measurement results of contact angle from different directions: (a) parallel direction; (b) vertical direction.

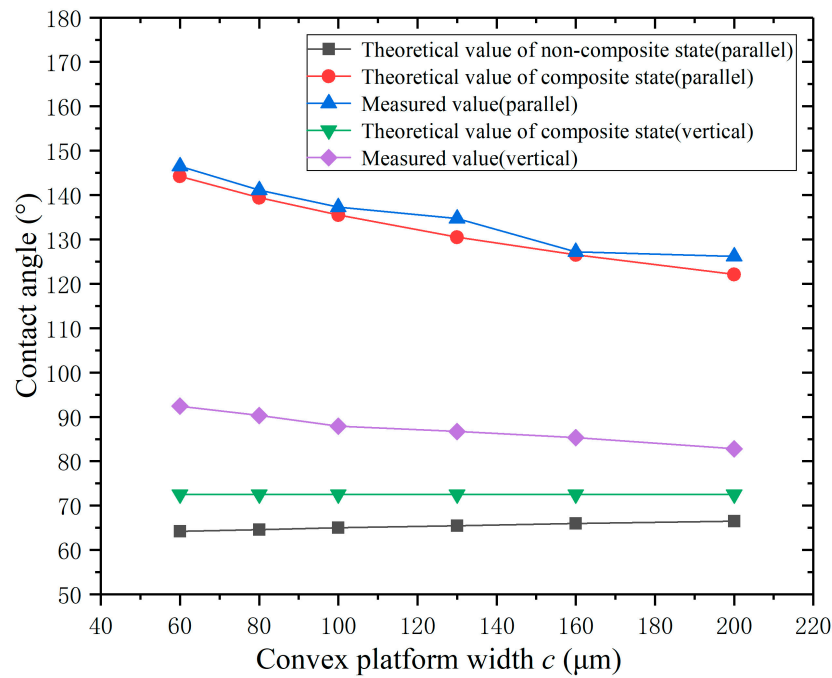


Figure 13. Variation curve of the contact angle between theory and measurement.

According to Figure 13, it can be seen that the measured contact angle in the parallel observation direction is always larger than that in the vertical observation direction, and the difference is from 54.1° to 43.4° . This is because the surface of the rectangular microgroove has obvious anisotropic wettability and there is a continuous groove wall in the parallel observation direction. If the water droplet expands to both sides, it requires a lot of energy [43]. The supporting effect of the groove wall makes the water droplets unable to spread to both sides, which produces the “pinning effect” [44]. However, the solid–liquid–gas three-phase contact line between the water droplet and the surface is like a straight line in the vertical observation direction, and there is no obstacle from the groove wall. Therefore, the contact mode in this direction is similar to that of the smooth surface. Water droplets are spread and expanded in the vertical direction, and the contact angle decreases continuously.

It is also found from Figure 13 that the variation trend of the theoretical contact angles of the composite state is consistent with the measured contact angles and the values are in good agreement with those in the parallel observation direction. The accuracy scope of

the prediction model is 96.8%~99.4%. Although the measured contact angles are always slightly larger than the theoretical contact angles, the maximum difference between them is only 4.2° , which comes from the surface of sample 4. The main reason for this difference is that, although the cutting parameters had been optimized before the preparation of the microstructure, there were two cutting methods of down-milling and up-milling on both sides of the microgroove when micro-milling the 316L stainless steel. In the down-milling process, the side edge of the micro milling cutter has the largest cutting thickness once it contacts the machined surface and the edge of the cutter was subjected to a large impact load. Therefore, the cutting process became very unstable, which led to an increase in the number of burrs [45]. By further amplifying the surface micro-morphology using scanning electron microscopy, it can be seen that the increase in the number of burrs will cause the micro-structural surface to cover at least two different scales of micro-textural features, as shown in Figure 14. These micro-aggregates made the surface morphology of samples rougher and more complicated, resulting in some cavities forming on the surface and improving the hydrophobicity. It can be seen from Figure 12a that a large number of air columns are trapped inside the microstructure, resulting in the composite contact mode between the water droplets and the sample surfaces. The analysis above indicates that the composite state prediction model is more in line with the contact state of water droplets in the parallel observation direction.

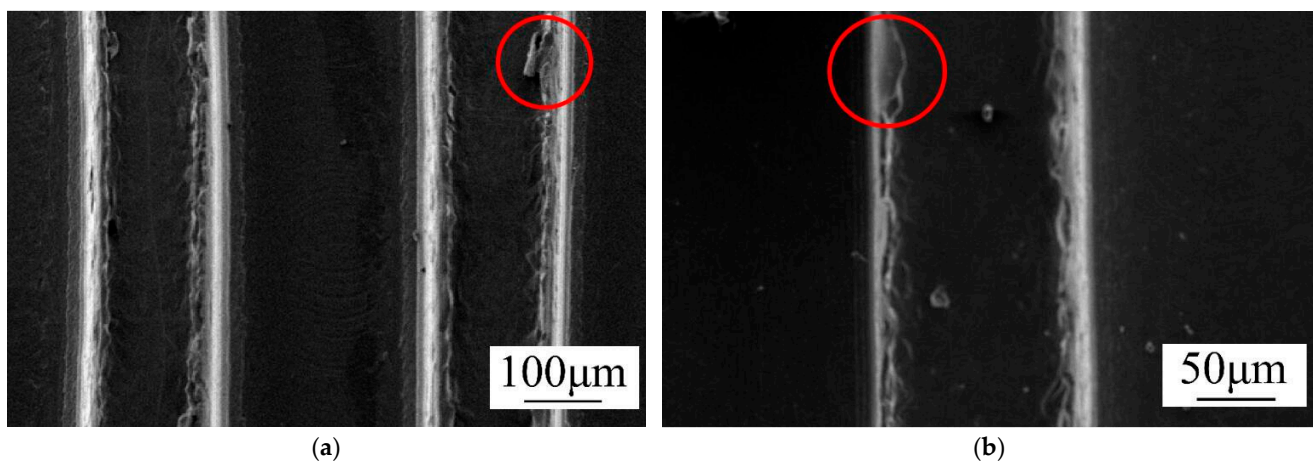


Figure 14. Scanning electron microscope (SEM) images of sample 4: (a) microtopography of the convex surface under 200 times zoom; (b) microtopography of the convex surface under 400 times zoom.

In addition, the theoretical contact angles of the composite state are equal to the contact angles of a smooth surface in the vertical observation direction. It can be seen from Figure 13 that the measured contact angles in this direction are always larger than the theoretical contact angles of the composite state, and the accuracy scope of the prediction model is 78.5%~87.6%. The reasons for this difference mainly come from two aspects. On the one hand, the multi-scale structure of the microgroove edge increased the opportunity for water droplets to form a composite state contact with the surface. On the other hand, the radial runout of the micro milling cutter made the actual dimension of the spacing width larger than the theoretical dimension. It is worth mentioning that as the width of the convex platform increases, the measured contact angle decreases and gradually tends toward the theoretical contact angle of the composite state. Therefore, the composite state contact angle model established in the vertical observation direction has a certain rationality.

In summary, the composite state model can be used to predict the contact angle, and reducing the width of the convex platform is beneficial to improving hydrophobicity. The prediction model is an important guide role for the preparation of oriented hydrophobic surfaces.

4. Conclusions

In this study, the contact angle prediction models of oriented hydrophobic surfaces were established based on the minimum Gibbs free energy and the effect of micro-structural dimension parameters on contact angle was analyzed. This result is useful for the design of controllable surfaces. Then, the precise periodic rectangular microgroove structure was obtained on 316L stainless steel by micro-milling, which is efficient and convenient. The prepared functional surface with directional hydrophobicity is expected to have potential applications in cardiovascular stents and droplet-oriented delivery. The contact angle value of the composite state prediction model is proved to be in good agreement with the actual results, and reducing the width of the convex platform will lead to an increase in the contact angle. This means that the micro-structural surface can form as many air columns as possible and form the composite contact state with water droplets by appropriately reducing the width of the convex platform, thereby exhibiting better hydrophobicity. The accuracy scope of the composite state prediction model in the parallel direction is 96.8%~99.4%. In particular, the contact angle in the parallel direction was 146.5° when the width of the convex platform was 60 μm, and the accuracy of the prediction model was as high as 98.4%. The composite prediction models of contact angle proposed in this study are reasonable and provide favorable guidance for the industrial production of oriented hydrophobic surfaces.

Author Contributions: Conceptualization, W.X. and Y.Z.; methodology, W.X. and Y.Z.; software, W.M.; validation, W.X. and Z.C.; formal analysis, J.P.; investigation, J.N.; resources, Z.C.; data curation, D.W.; writing—original draft preparation, W.X.; writing—review and editing, W.X. and Z.C.; visualization, W.X.; supervision, Z.C.; project administration, Z.C.; funding acquisition, Y.Z. All authors have read and agreed to the published version of the manuscript.

Funding: This research received no external funding.

Institutional Review Board Statement: Not applicable.

Informed Consent Statement: Not applicable.

Data Availability Statement: The data presented in this study are available in article.

Acknowledgments: The authors acknowledge the technical staff of our research laboratory for their assistance in carrying out the experiments.

Conflicts of Interest: The authors declare no conflict of interest.

References

1. Chen, C.H.; Cheng, I.C.; Chen, J.Z. Facile method to convert petal effect surface to lotus effect surface for superhydrophobic polydimethylsiloxane. *Surf. Interfaces* **2022**, *30*, 101901. [[CrossRef](#)]
2. Barthlott, W.; Neinhuis, C. Purity of the sacred lotus, or escape from contamination in biological surfaces. *Planta* **1997**, *202*, 1–8. [[CrossRef](#)]
3. Cao, Z.Y.; Ding, W.Y.; Ma, Z.W.; Wang, B.F.; Wang, Z.W. Research on the hydrophobicity of square column structures on monocrystalline silicon fabricated using micro-machining. *Micromachines* **2019**, *10*, 763. [[CrossRef](#)]
4. Qian, W.; Hua, Y.Q.; Chen, R.F.; Xu, P.; Yang, J. Fabrication of superhydrophobic nickel-aluminum bronzes using picosecond laser for enhancing anti-corrosion property. *Mater. Lett.* **2020**, *268*, 127570. [[CrossRef](#)]
5. Sun, J.F.; Wang, W.Q.; Liu, Z.; Li, B.; Xing, K.F.; Yang, Z. Study on selective laser melting 316L stainless steel parts with superhydrophobic surface. *Appl. Surf. Sci.* **2020**, *533*, 147445. [[CrossRef](#)]
6. Bixler, G.D.; Theiss, A.; Bhushan, B.; Lee, S.C. Anti-fouling properties of microstructured surfaces bio-inspired by rice leaves and butterfly wings. *J. Colloid Interface Sci.* **2014**, *419*, 114–133. [[CrossRef](#)]
7. Zhang, J.; Li, G.L.; Li, D.H.; Zhang, X.R.; Li, Q.H.; Liu, Z.H.; Fang, Y.J.; Zhang, S.; Man, J. In vivo blood-repellent performance of a controllable facile-generated superhydrophobic surface. *ACS Appl. Mater. Interfaces* **2021**, *13*, 29021–29033. [[CrossRef](#)]
8. Luo, Y.H.; Wang, X.D.; Liu, G.; Wang, J.S.; Song, W. Anisotropic wetting and fluidic phenomena on biological texture and hydrodynamic experiments testing on different low viscous resistance surfaces. *Adv. Eng. Mater.* **2016**, *18*, 869–876. [[CrossRef](#)]
9. Tuo, Y.J.; Zhang, H.F.; Rong, W.T.; Jiang, S.Y.; Chen, W.P.; Liu, X.W. Drag reduction of anisotropic superhydrophobic surfaces prepared by laser etching. *Langmuir* **2019**, *35*, 11016–11022. [[CrossRef](#)] [[PubMed](#)]
10. Ghosh, A.; Ganguly, R.; Schutzius, T.M.; Megaridis, C.M. Wettability patterning for high-rate, pumpless fluid transport on open, non-planar microfluidic platforms. *Lab Chip*. **2014**, *14*, 1538–1550. [[CrossRef](#)]

11. De Marco, C.; Eaton, S.M.; Suriano, R.; Turri, S.; Levi, M.; Ramponi, R.; Cerullo, G.; Osellame, R. Surface properties of femtosecond laser ablated PMMA. *ACS Appl. Mater. Interfaces* **2010**, *2*, 2377–2384. [[CrossRef](#)]
12. Bartlett, K.; Movafaghi, S.; Dasi, L.P.; Kota, A.K.; Popat, K.C. Antibacterial activity on superhydrophobic titania nanotube arrays. *Colloids Surf. B Biointerfaces* **2018**, *166*, 179–186. [[CrossRef](#)] [[PubMed](#)]
13. Zhou, X.; Xue, W.; Liu, W.; Zhu, D.; Cao, Y. Quadri-directionally anisotropic droplets sliding surfaces fabricated by selective laser texturing of aluminum alloy plates. *Appl. Surf. Sci.* **2020**, *509*, 145406. [[CrossRef](#)]
14. Lian, Z.; Xu, J.; Yu, Z.; Yu, P.; Yu, H. A simple two-step approach for the fabrication of bio-inspired superhydrophobic and anisotropic wetting surfaces having corrosion resistance. *J. Alloy. Compd.* **2019**, *793*, 326–335. [[CrossRef](#)]
15. Fang, Y.; Yong, J.L.; Chen, F.; Huo, J.L.; Yang, Q.; Zhang, J.Z.; Hou, X. Bioinspired fabrication of bi/tridirectionally anisotropic sliding superhydrophobic PDMS surfaces by femtosecond laser. *Adv. Mater. Interfaces* **2018**, *5*, 1701245. [[CrossRef](#)]
16. Xu, J.K.; Hou, Y.G.; Lian, Z.X.; Yu, Z.J.; Wang, Z.B.; Yu, H.D. Bio-inspired design of bi/tridirectionally anisotropic sliding superhydrophobic titanium alloy surfaces. *Nanomaterials* **2020**, *10*, 2140. [[CrossRef](#)]
17. Long, J.Y.; Fan, P.X.; Jiang, D.F.; Han, J.P.; Lin, Y.; Cai, M.Y.; Zhang, H.J.; Zhong, M.L. Anisotropic sliding of water droplets on the superhydrophobic surfaces with anisotropic groove-like micro/nano structures. *Adv. Mater. Interfaces* **2016**, *3*, 1600641. [[CrossRef](#)]
18. Zhu, D.F.; Li, X.; Zhang, G.; Zhang, X.; Zhang, X.M.; Wang, T.Q.; Yang, B. Mimicking the rice leaf-from ordered binary structures to anisotropic wettability. *Langmuir* **2010**, *26*, 14276–14283. [[CrossRef](#)] [[PubMed](#)]
19. Park, H.; Sun, G.Y.; Kim, C.J. Superhydrophobic turbulent drag reduction as a function of surface grating parameters. *J. Fluid Mech.* **2014**, *747*, 722–734. [[CrossRef](#)]
20. Xiao, X.Y.; Xie, W.; Ye, Z.H. Preparation of corrosion-resisting superhydrophobic surface on aluminium substrate. *Surf. Eng.* **2019**, *35*, 411–417. [[CrossRef](#)]
21. Tan, J.Y.; Hao, J.J.; An, Z.Q.; Liu, C.S. Simple fabrication of superhydrophobic nickel surface on steel substrate via electrodeposition. *Int. J. Electrochem. Sci.* **2017**, *12*, 40–49. [[CrossRef](#)]
22. Lin, C.W.; Chung, C.J.; Chou, C.M.; He, J.L. Morphological effect governed by sandblasting and anodic surface reforming on the super-hydrophobicity of AISI 304 stainless steel. *Thin Solid Films* **2016**, *620*, 88–93. [[CrossRef](#)]
23. Wang, Y.T.; Zhao, X.Y.; Ke, C.J.; Yu, J.; Wang, R. Nanosecond laser fabrication of superhydrophobic Ti6Al4V surfaces assisted with different liquids. *Colloid Interface Sci. Commun.* **2020**, *35*, 100256. [[CrossRef](#)]
24. Bae, W.G.; Song, K.Y.; Rahmawan, Y.; Chu, C.N.; Kim, D.; Chung, D.K.; Suh, K.Y. One-step process for superhydrophobic metallic surfaces by wire electrical discharge machining. *ACS Appl. Mater. Interfaces* **2012**, *4*, 3685–3691. [[CrossRef](#)]
25. Rahman, M.A.; Jacobi, A.M. Wetting behavior and drainage of water droplets on microgrooved brass surfaces. *Langmuir* **2012**, *28*, 13441–13451. [[CrossRef](#)] [[PubMed](#)]
26. Wei, D.S.; Wang, J.G.; Liu, Y.; Wang, D.W.; Li, S.Y.; Wang, H.Y. Controllable superhydrophobic surfaces with tunable adhesion on Mg alloys by a simple etching method and its corrosion inhibition performance. *Chem. Eng. J.* **2021**, *404*, 126444. [[CrossRef](#)]
27. Wang, H.Y.; Zhu, Y.X.; Hu, Z.Y.; Zhang, X.G.; Wu, S.Q.; Wang, R.; Zhu, Y.J. A novel electrodeposition route for fabrication of the superhydrophobic surface with unique self-cleaning, mechanical abrasion and corrosion resistance properties. *Chem. Eng. J.* **2016**, *303*, 37–47. [[CrossRef](#)]
28. Mokhtari, S.; Karimzadeh, F.; Abbasi, M.H.; Raeissi, K. Development of super-hydrophobic surface on Al 6061 by anodizing and the evaluation of its corrosion behavior. *Surf. Coat. Technol.* **2017**, *324*, 99–105. [[CrossRef](#)]
29. Volpe, A.; Covella, S.; Gaudioso, C.; Ancona, A. Improving the laser texture strategy to get superhydrophobic aluminum alloy surfaces. *Coatings* **2021**, *11*, 369. [[CrossRef](#)]
30. Chen, Z.; Yan, Z.J.; Zhou, H.B.; Han, F.L.; Zhao, L.H.; Yan, H.Z. One-step fabrication of the wear-resistant superhydrophobic structure on SiCp/Al composite surface by WEDM. *Surf. Coat. Technol.* **2021**, *409*, 126876. [[CrossRef](#)]
31. Sun, R.Y.; Li, Z.; Zhao, J.; Mo, J.L.; Pan, Y.J.; Luo, D.B. Facile fabrication of durable superhydrophobic aluminum alloy surfaces by HS-WEDM and chemical modification. *Nano* **2021**, *16*, 2150133. [[CrossRef](#)]
32. Zhang, X.; Wan, Y.; Ren, B.; Wang, H.W.; Yu, M.Z.; Liu, A.Q.; Liu, Z.Q. Preparation of superhydrophobic surface on titanium alloy via micro-milling, anodic oxidation and fluorination. *Micromachines* **2020**, *11*, 316. [[CrossRef](#)]
33. Otitoju, T.A.; Ahmad, A.L.; Ooi, B.S. Superhydrophilic (superwetting) surfaces: A review on fabrication and application. *J. Ind. Eng. Chem.* **2017**, *47*, 19–40. [[CrossRef](#)]
34. Nguyen, H.H.; Tieu, A.K.; Wan, S.H.; Zhu, H.T.; Pham, S.T.; Johnston, B. Surface characteristics and wettability of superhydrophobic silanized inorganic glass coating surfaces textured with a picosecond laser. *Appl. Surf. Sci.* **2021**, *537*, 147808. [[CrossRef](#)]
35. Wang, H.; Chi, G.X.; Li, L.; Gong, S.R.; Zhu, J.L.; Tian, C.; Wang, Y.K.; Wang, Z.L. Numerical calculation of apparent contact angles on the hierarchical surface with array microstructures by wire electrical discharge machining. *Langmuir* **2021**, *37*, 1768–1778. [[CrossRef](#)] [[PubMed](#)]
36. Young, T. An essay on the cohesion of fluids. *Philos. Trans. R. Soc. Lond.* **1805**, *95*, 65–87.
37. Wenzel, R.N. Resistance of solid surfaces to wetting by water. *Ind. Eng. Chem.* **1936**, *28*, 988–994. [[CrossRef](#)]
38. Cassie, A.B.D.; Baxter, S. Wettability of porous surfaces. *Trans. Faraday Soc.* **1944**, *40*, 546–551. [[CrossRef](#)]
39. Quéré, D. Non-sticking drops. *Rep. Prog. Phys.* **2005**, *68*, 2495. [[CrossRef](#)]
40. Extrand, C.W. Criteria for ultralyophobic surfaces. *Langmuir* **2004**, *20*, 5013–5018. [[CrossRef](#)]
41. Martellotti, M.E. An analysis of the milling process, part ii—Down milling. *J. Fluids Eng.* **1945**, *67*, 233–251. [[CrossRef](#)]

42. Thevenot, V.; Arnaud, L.; Dessein, G.; Cazenave-Larroche, G. Integration of dynamic behaviour variations in the stability lobes method: 3D lobes construction and application to thin-walled structure milling. *Int. J. Adv. Manufact. Technol.* **2006**, *27*, 638–644. [[CrossRef](#)]
43. Kong, L.B.; Cheung, C.F.; To, S.; Cheng, C.T. Modeling and characterization of generation of 3D micro-structured surfaces with self-cleaning and optical functions. *Optik* **2013**, *124*, 2848–2853. [[CrossRef](#)]
44. Neuhaus, S.; Spencer, N.D.; Padeste, C. Anisotropic wetting of microstructured surfaces as a function of surface chemistry. *ACS Appl. Mater. Interfaces* **2012**, *4*, 123–130. [[CrossRef](#)]
45. Hajiahmadi, S. Burr size investigation in micro milling of stainless steel 316L. *Int. J. Lightweight Mater. Manufact.* **2019**, *2*, 296–304. [[CrossRef](#)]

Disclaimer/Publisher’s Note: The statements, opinions and data contained in all publications are solely those of the individual author(s) and contributor(s) and not of MDPI and/or the editor(s). MDPI and/or the editor(s) disclaim responsibility for any injury to people or property resulting from any ideas, methods, instructions or products referred to in the content.